Epithelial layer fluidization by curvature-induced unjamming

Margherita De Marzio,[1,2] Amit Das,[3] Jeffrey J. Fredberg,[2] and Dapeng Bi[4,*]

[1]*Channing Division of Network Medicine, Brigham and Women's Hospital and Harvard Medical School, Boston, MA 02115, USA*
[2]*Harvard T.H. Chan School of Public Health, Boston, MA 02115, USA*
[3]*Department of Biochemical Engineering and Biotechnology, IIT Delhi, New Delhi, India*
[4]*Department of Physics, Northeastern University, Boston, MA 02115, USA*

The transition of an epithelial layer from a stationary, quiescent state to a highly migratory, dynamic state is required for wound healing, development, and regeneration. This transition, known as the unjamming transition (UJT), is responsible for epithelial fluidization and collective migration. Previous theoretical models have primarily focused on the UJT in flat epithelial layers, neglecting the effects of strong surface curvature that is characteristic of epithelial tissues *in vivo*. In this study, we investigate the role of surface curvature on tissue plasticity and cellular migration using a vertex model embedded on a spherical surface. Our findings reveal that increasing curvature promotes epithelial unjamming by reducing the energy barriers to cellular rearrangements. Higher curvature favors cell intercalation, mobility, and self-diffusivity, resulting in epithelial structures that are malleable and migratory when small, but become more rigid and stationary as they grow. As such, curvature-induced unjamming emerges as a novel mechanism for epithelial layer fluidization. Our quantitative model proposes the existence of a new, extended, phase diagram wherein local cell shape, cell propulsion, and tissue geometry combine to determine the epithelial migratory phenotype.

To heal a wound, remodel a tissue, or invade into surrounding structures, the confluent epithelial layer transitions from a state wherein constituent cells are sedentary and quiescent into one wherein these cells become strikingly migratory and dynamic [1, 2]. In certain contexts this phenotypic switch has been interpreted within the novel paradigm known as the unjamming transition (UJT) [3–12]. In the jammed phase, cellular rearrangements become rare because each cell becomes virtually locked in place by its neighbors, thus leading to tissue homeostasis and rigidity. In the unjammed phase, each cell can move cooperatively and collectively with its neighboring cells, thus leading to epithelial fluidity, mobility, and malleability [13–16].

Theoretical models to date have characterized the UJT as it might occur in the epithelial layer that resides upon flat surfaces [17–25]. By contrast, the epithelial layer *in vivo* typically resides upon surfaces that are strongly curved. By the word strong here we mean cases in which the radius of surface curvature can become as small as several cell diameters. These include, for example, spherical pulmonary alveoli, tubular small airways, and ellipsoidal embryos [26–28]. It has been shown experimentally that such curved geometries alter epithelial plasticity in a non-trivial manner: topological defects and out-of-plane forces impact cell packing and cytoskeletal organization [26, 27, 29–36]; additionally, curvature influences migration and cooperativity, inducing coherent rotational motions and cell alignment [29, 30, 33, 34, 36].

Previous theoretical models have studied tissue plasticity of curved epithelia in the contexts of the developing neural tube, the fly leg disc, and the mouse optical cup [37–41]. However, these particular geometries make it difficult to isolate the intrinsic effects of surface curvature from those induced by topological constraints. As such, the mechanistic role of surface curvature on cell packing, mobility, and the resulting epithelial jamming dynamics remains poorly understood.

To fill that gap, here we embed a vertex model (VM) [5, 17–20, 42, 43] onto a spherical surface. Using that model we investigate jamming dynamics in physiological ranges of cell density and surface curvature. Our results show that as surface curvature progressively increases, energy barriers to cellular rearrangements progressively decrease. In the presence of cellular propulsion, increasing curvature therefore favors increased cellular migration, larger self-diffusivity, and more frequent intercalation events.

This model is significant in at least three ways. Firstly, it suggests that the developing curved structure would tend to be unjammed, fluid-like, and malleable when small but become progressively more jammed, solid-like, and rigid as it grows. Secondly, it points to the existence of a novel mechanism of epithelial layer fluidization, namely, curvature-induced unjamming. Finally, it provides a quantitative tool for thought to better understand the interplay of cell shape, cell propulsion, and tissue geometry in contributing to the migratory phenotype *in vivo*.

The Spherical Vertex Model—We embed a 3D apical vertex model [18, 19, 37, 38, 44, 45] on a spherical topology (Fig.1). This framework is based on the observation that epithelial cells tend to tile the surface in a confluent polygonal array while maintaining their columnar structure [37, 38]. In this geometry, we specify the apical surface of cells by the location of vertices, which are constrained to move on the surface of the sphere. Cell edges are defined by the geodesic curve connecting two adjacent vertices. As used previously for flat surfaces, we define the mechanical energy of the system by the energy function $E = \sum_{i=1}^{N} [K_A(A_i - A_0)^2 + K_P(P_i - P_0)^2]$. A_i and P_i are the apical area and perimeter of the *i-th* cell and are calculated based on the geodesic polygons enclosed by the vertex positions $\{\mathbf{r}_i\}$ [18, 20, 37, 45, 46]. A_0 and P_0 represent the cell preferred area and perimeter, and are homogeneous across all N cells. K_A and K_P are the elastic moduli associated with deformations of the area and perimeter, respectively. As described previously, this energy func-

tion accounts for the three-dimensional cell incompressibility [45, 47], tissue bulk and actomyosin cortex elasticities [45–48], and the interplay between cell-cell adhesion and cortical tension [18, 25, 43, 45, 46, 48, 49]. Here we set the preferred cell area to be the average per cell $A_0^i = \bar{A}$. By choosing $K_P\bar{A}$ as the energy unit and $\sqrt{\bar{A}}$ as the length unit, the energy functional reduces to the nondimensional equation:

$$\varepsilon = \sum_{i=1}^{N} [k_A(a_i - 1)^2 + (p_i - p_0)^2], \qquad (1)$$

where $a_i = A_i/\bar{A}$ and $p_i = P_i/\sqrt{\bar{A}}$ are the rescaled area and perimeter of the i-th cell, $k_A = K_A\bar{A}/K_P$ is the rescaled cell area elasticity, and $p_0 = P_0/\sqrt{A_0}$ is a dimensionless target shape index.

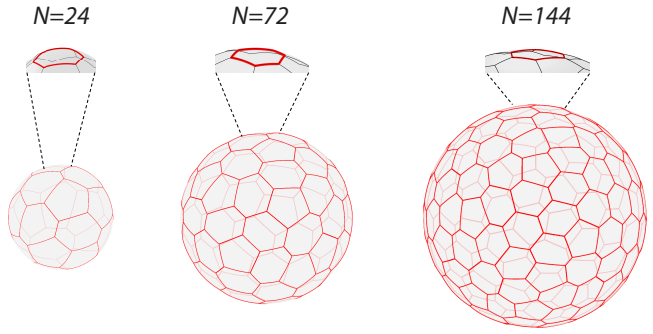

FIG. 1. Schematic of the spherical VM. Each cell has unit area on average. Therefore, spheres with lower number of cells N exhibit higher surface curvature.

We examine this system at various radii of curvature while isolating the influence of number density. To achieve this, the sphere radius R is chosen such that each cell has unit area on average, i.e. $R = \sqrt{N/4\pi}$. Consequently, spherical surfaces with fewer cells N exhibit higher curvature (Fig.1). Different system sizes $N = 36 - 300$ are analyzed, corresponding to radii of curvature in the range of $1.69 - 4.9$ times the mean cell size. This constitutes a physiologically relevant range experienced by cells in curved epithelia [36]. A range of choices for the shape index p_0 is studied at each N. For each parameter choice, we use a combination of the first-order conjugate-gradient and second-order Newton's method to find the nearest local energy minima [50, 51] (see Supplementary Materials [SM]). Using the same energy minimization scheme, we simulate also a flat VM of $N = 300$ cells in the same range of p_0.

Curvature promotes epithelial fluidity— We first study how substrate geometry influences tissue rigidity. In the case of flat surfaces, the vertex model predicts a rigidity transition at the critical value $p_0 = p_0^* \sim 3.81$ [18–20, 25, 52]. This transition is driven by a percolation transition of the tissue's tension network, defined as the network of edges with tension $\tau > 0$ [25, 52, 53]. We examine the spatial organization of the tension network in the spherical VM (see SM for analysis details).

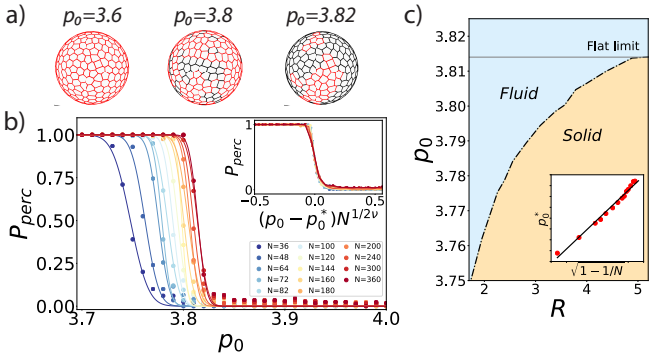

FIG. 2. a) Snapshots of the sphere's tension network at $N = 300$ and $p_0 = 3.6$ (left), $p_0 = 3.8$ (central), and $p_0 = 3.82$ (right). Red edges have finite tension. b) Probability of tension percolation P_{perc} versus p_0 for different N. $P_{perc}(p_0, N)$ is well described by the error function $1/2 - 1/2erf[(p_0 - \mu_N)/(\sqrt{2}\sigma_N)]$ (solid lines). When P_{perc} is rescaled by finite-size effects ($N^{1/2\nu}$, $\nu = 0.6$) and shifted by the percolation threshold $p_0^*(N)$, the rescaled P_{perc} collapses onto a single curve (inset). c) Glassy phase diagram of the spherical VM. The onset of rigidity $p_0^*(R)$ increases with increasing radius R, and hence decreasing curvature (dashed line). Below $p_0^*(R)$ (orange area), the tension network percolates and the tissue is solid-like. Above $p_0^*(R)$ (blue area), the tension network becomes disconnected and the tissue is fluid-like. (Inset) In agreement with our mean-field model, p_0^* increases proportionally to $\sqrt{1 - 1/N}$.

At fixed curvature, the tension network displays a behavior analogous to the flat surface. At lower p_0 (left panel of Fig.2a), the network forms a system-spanning structure and the tissue is completely rigid. By increasing p_0, the network segregates progressively into disconnected components that are reminiscent of a fluid-like phase [25] (central and right panel of Fig.2a). We quantify this behavior at different curvatures by calculating the probability of tension percolation P_{perc} at various p_0 and N (Fig.2b, see SM for details). Similar to the flat tissue, P_{perc} decays with p_0 as an error function. P_{perc} becomes sharper and more heavy-tailed by increasing N, as expected due to finite-size effects [25]. Increasing N also shifts P_{perc} towards higher values of p_0, suggesting a role of curvature that goes beyond finite-size scaling. In confirmation of this role, the tension percolation threshold $p_0^*(R)$, and hence the onset of rigidity, increases by increasing the radius of curvature R (Fig.2c, see SM for calculation details). In the zero-curvature limit $R \to \infty$, $p_0^*(R)$ approaches the flat limit $p_0^*(\infty) \sim 3.814$. Notably, P_{perc} collapses onto a single curve after shifting by $p_0^*(R)$ and rescaling by the finite-size scaling law $N^{1/2\nu}$, with $\nu = 0.6$ (Inset of Fig.2b). These results indicate that curvature promotes tissue fluidization.

Curvature-induced epithelial fluidity arises from lowering of energy barriers for cellular rearrangements— To gain mechanistic insights on the curvature-induced fluidization, we examine the mechanical response of the tissue to external perturbations. Under confluency, tissue fluidity is driven by cells' ability to rearrange via T1 topological swaps (Fig.3a) [54–60]. We hypothesize that tissue curvature impacts rigid-

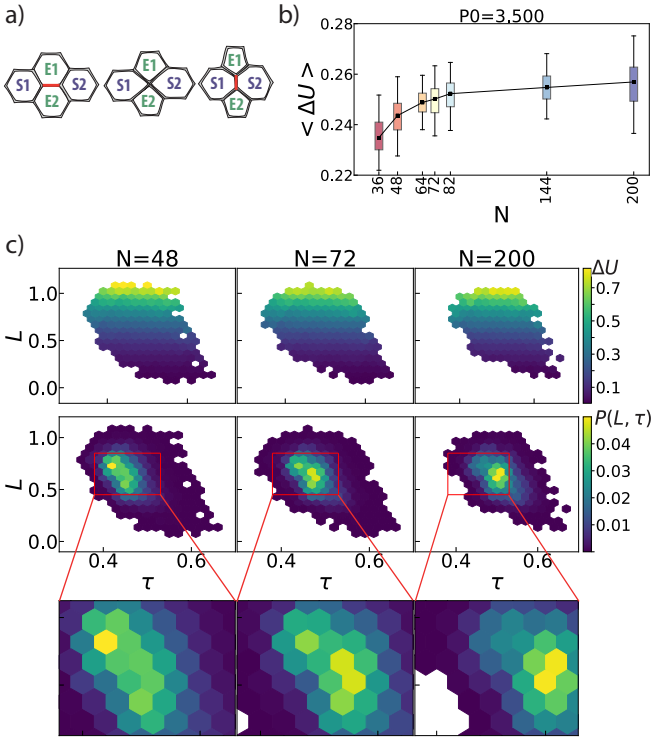

FIG. 3. a) Schematic of a T1 transition. Left: Cells E1 and E2 share initially an edge (highlighted in orange). Center: the edge is collapsed into a four-fold vertex. Right: A new edge is created between cells S1 and S2 (highlighted in orange). b) T1's energy barriers ΔU versus N at fixed $p_0 = 3.5$. The black line indicates the average $\langle \Delta U \rangle$. c) Distributions of energy barriers (ΔU), edge lengths (L), and edge tensions (τ) at $N = 48$, $N = 72$, and $N = 200$ and $p_0 = 3.5$. The ΔU associated with edges with same length and tension show no significant changes with curvature (top panels). Conversely, the density distribution $P(L,\tau)$ of edge lengths and tensions (central panels) shifts toward smaller L and larger τ with larger N (magnified in the bottom panels).

ity by affecting the energy required to execute a T1 transition. To test this, we study how the T1's energy barriers ΔU change with curvature. ΔU is defined as the energy cost to collapse an edge into a fourfold vertex (see SM for details). We find that ΔU decreases on average with increasing curvature (Fig.3b). Analysis of ΔU as a function of the edge tension τ and length L reveals additional insights (Fig.3c). Similar to flat surfaces [18, 19, 43, 61], $\Delta U(L,\tau)$ increases with L. However, $\Delta U(L,\tau)$ shows no significant changes between edges with same (L,τ) values but different curvature (top panels of Fig.3c). This suggests that T1 transitions in curved tissues do not incorporate any bending effect.

To explain this behavior, we delve into the functional mechanism of T1 transitions. During an edge collapse, tissue energy is impacted by two effects (see details in SM): 1) the pure topological rearrangement of the connectivity network; and 2) the subsequent relaxation of the surrounding vertices to reach a new stable configuration. We study these contributions separately. Interestingly, the relaxation and topological terms are positively correlated as $\Delta U_{rel} \sim \eta \Delta U_{top}$, with η being independent of N (see SM).

The functional dependence of ΔU_{top} from (L,τ) can be predicted by developing a simple geometric ansatz. When an edge is collapsed, $\Delta U_{top} = \Delta U_{per} + \Delta U_{area}$ is defined only by the changes in area ΔU_{area} and perimeter ΔU_{per} of the four neighboring cells involved in the T1 transition (see SM for details). In a mean-field approximation where all four cells are initially regular hexagons, ΔU_{per} and ΔU_{area} can be derived analytically as (see SM for derivation):

$$\Delta U_{per} = AL^2 + BL + C\tau L \qquad \Delta U_{area} = [\sin(\frac{4}{6}\pi)L^2]^2. \quad (2)$$

The coefficients A, B, and C are determined by the initial geometry of the four cells involved in the T1 (see SM). Similar to previous reports [18, 19, 61], Eq.2 includes a quadratic dependence of ΔU_{per} on L. Our model reveals also a linear dependence on the edge tension that is modulated by L. It follows that T1 transitions are energetically penalized in both longer and more tense edges.

By combining the relationship between ΔU_{rel} and ΔU_{top} with Eq.2, we recapitulate the dependence of ΔU from L and τ. At fixed $\tau = \tau_0$, $\Delta U(L,\tau)$ collapses on a single master curve that is independent of curvature and is well described by our mean-field model (see Supplementary Figures in SM). Our predictions hold also on flat surfaces (see SM), confirming the universality of Eq.2.

Our findings suggest that edge length and tension act together as reaction coordinates of the T1 process, much like temperature and energy in Arrhenius processes. Importantly, surface curvature does not impact the T1's dependence on these coordinates. Conversely, curvature alters the equilibrium configuration of edge lengths and tensions (central row of Fig.3c). The density distribution $P(L,\tau)$ shifts towards longer and less tense edges with increasing curvature. This suggests that curvature-induced fluidization does not stem from local changes in the individual T1 mechanism, but rather from global changes in the edge network.

In the absence of cell motility, curvature of the jammed layer impacts the distributions of edge lengths and edge tensions—To understand how changes in the cell junctional network impact tissue rigidity, we investigate $P(L,\tau)$ in more detail. In agreement with our percolation analysis, the tension distribution $P(\tau)$ shifts towards larger τ values by increasing N (Fig.4a). The distribution of edge lengths $P(L)$ exhibits a more intriguing behavior. On flat surfaces, $P(L)$ has been traditionally reported as a Gaussian [19]. On the spherical layer, however, $P(L)$ appears as the sum of multiple Gaussians $e^{(x-\mu)/\sigma}$ (Fig.4b). These Gaussians coincide with distinct contact topologies around the edge. Indeed, we find (μ,σ) to be parametric in the quantity $Q = 6 - Z_{S1} + 6 - Z_{S2}$, where Z_{S1} and Z_{S2} are the number of neighbors of cells S1 and S2 (Fig.3a). Edges are shorter at higher values of Q, which corresponds to $S1, S2$ pairs with fewer neighbors. Notably, we recover this behavior also on flat surfaces (see SM). A monotonic decrease of ΔU with Q has been previously reported on

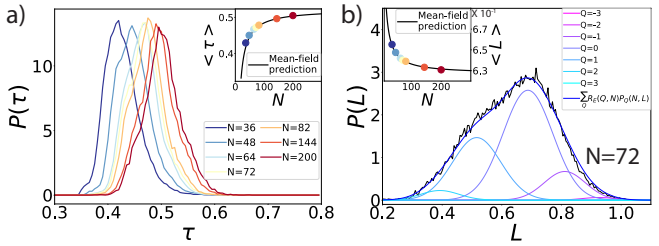

FIG. 4. a) Density distribution $P(\tau)$ of edge tensions for spheres with different N. (Inset) Average edge tension $\langle\tau(N)\rangle$ versus N. Solid line corresponds to Eq.4. b) Density distribution $P(L)$ of edge lengths at $N = 72$ (black line). Colored solid lines correspond to Gaussian fits of the densities $P_Q(L)$. The blue solid line corresponds to the weighted sum of the Gaussian fits $\sum_Q R_E(Q,N)P_Q(N,L)$, where $R_E(Q,N)$ is the fraction of edges with given Q over the total. (Inset) Average edge length $\langle L(N)\rangle$ versus N. Solid line corresponds to Eq.3, with $P_{flat} = 3.76$ equal to the average perimeter at the largest $N = 360$.

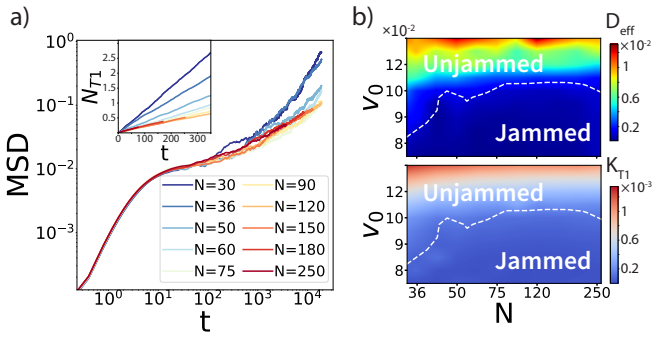

FIG. 5. a) Average mean-square displacement (MSD) of individual cells vs time. Colors represent different radii of curvature. (Inset) Cumulative count of T1 transitions per junction as a function of time. b) Heatmaps of the diffusion coefficient D_{eff} (upper panel) and T1's rate k_{T1} (lower panel) as a function of N and cell velocity v_0. The dashed line represents the motility-driven transition line $v_0^*(N)$, defined as the (N, v_0) values at which $D_{eff} = 0.001$ [20, 63].

flat surfaces [19]. Our results provide a mechanistic insight into this dependence: cell edges tend to be shorter at larger Q, thus decreasing the energetic cost for cellular rearrangements.

Analysis of $P_Q(L)$ at different radii of curvature shows that μ_Q decreases with N, while the distribution of Q follows a non-monotonic behavior (see SM). This leads to an average increase of edge lengths with increasing curvature (inset of Fig.4b). As such, curvature affects the spatial (edge lengths) and mechanical (edge tensions) configuration of the cell network in opposite ways.

This effect can be explained through geometric arguments. The perimeter P of a spherical polygon is related to its equivalent P_{flat} on the flat surface via the identity $P(N) = P_{flat}\sqrt{1-\frac{1}{N}}$ (see SM for derivation). By combining this identity with the Gauss-Bonnet theorem [62], the average edge length $\langle L\rangle$ and tension $\langle\tau\rangle$ can be written as:

$$\langle L\rangle \approx \left\langle \frac{P}{Z}\right\rangle \approx \frac{\langle P_{flat}\rangle\sqrt{1-\frac{1}{N}}}{6-\frac{12}{N}} \tag{3}$$

$$\langle\tau\rangle \approx 2\langle P\rangle - 2P_0 = \tau_{flat} + A_\tau\left(-1+\sqrt{1-\frac{1}{N}}\right), \tag{4}$$

where $\tau_{flat} = 2\langle P_{flat}\rangle - 2P_0$ and $A_\tau = 2\langle P_{flat}\rangle$. Both Eq.3 and Eq.4 recapitulate our simulations results (insets of Fig.4a and Fig.4b). Eq.4 reflects the fact that cells with the same area and higher curvature have smaller perimeters, and hence lower edge tensions on average. However, the average cell coordination number is lower at higher curvatures. The combination of these two effects leads to longer edges with increasing curvature.

Our findings demonstrate that curvature tunes tissue rigidity through the competition of topological and mechanical changes. On one hand, longer edges penalize cell rearrangements; on the other hand lower intercellular tensions favor cell intercalation. This latest effect dominates tissue rigidity, leading to mechanical states that are more fluid-like at higher curvatures. Indeed, our mean-field model predicts that the tension-dependent energy term $L\tau$ of Eq.2 vanishes at $p_0^*(N) \propto \sqrt{1-1/N}$ (see SM). In agreement with this prediction, the rigidity transition point $p_0^*(N)$ increases proportionally to $\sqrt{1-1/N}$ (inset of Fig.2c).

In the presence of cell motility, curvature promotes cellular migration— We further investigate how curvature affects tissue fluidity in presence of cell motility. To do so, we study the dynamics of a motile cell monolayer on the spherical surface.

Similar to our recent work on the sphere [36], we consider the dynamics of cells under the influence of substrate frictional drag. In this description, the change rate of position $\vec{r}_i$ of the i-th vertex obeys the overdamped equation of motion:

$$\Gamma\frac{d\vec{r}_i}{dt} = \vec{F}_i^{int} + v_0\hat{n}_i, \tag{5}$$

where Γ is the viscous damping coefficient due to cell-substrate interactions. The forces on the vertices arise from two sources: interactions between cells mediated by cell-cell contacts ($\vec{F}_i^{int}$) and cellular tractions applied on the substrate ($v_0\hat{n}_i$). The first contribution is determined by the spatial gradient of tissue mechanical energy defined in Eq.1, whereas the second contribution is modelled as an active motility force applied on vertex i with constant strength v_0. The direction of the traction force $\hat{n}_i$ is determined by the sum of polarization vectors of the three cells sharing the vertex. The implementation of individual cell polarization is similar to other self-propelled particle models on spherical geometries [64]. Individual cell polarization vectors undergo rotational diffusion with rate D_r [65, 66] (see SM for details).

We first analyze the cell dynamics of the spherical layer at fixed $v_0 = 0.09$ and $p_0 = 3.65$. The average cell mean-square displacement $\langle\Delta r^2(t)\rangle$ displays three temporal regimes that are reminiscent of glassy dynamics (Fig. 5a): an early-time ballistic regime, an intermediate switching regime that resembles a plateau, and a long-time diffusive regime. For each N,

we calculate the self-diffusivity coefficient D_{eff} in units of the free diffusion constant D_0 of an isolated cell. D_{eff} is defined as $D_{eff} = D_s/D_0$, where $D_s = \lim_{t\to\infty}\langle\Delta r^2(t)\rangle/(4t)$ and $D_0 = v_0^2/(2D_r)$ [20]. D_{eff} shows a strong dependence on curvature, exhibiting higher values at lower N (see Supplementary Figure in SM). Similarly, the cumulative number N_{T1} of T1 transitions per junction over time is higher in spheres with higher curvature (inset of Fig.5a).

We further measure D_{eff} and the rate of T1 transitions k_{T1} for several combinations of v_0 and N. At fixed N, the spherical monolayer shows a motility-driven transformation from a solid-like to a fluid-like state (Fig.5b). Notably, surface curvature modulates the cell motility threshold v_0^* at which this transition occurs. Indeed, v_0^* increases gradually with N (Fig.5b). This indicates that, all other factors being equal, the epithelial layer is more fluid-like and unjammed when it resides upon more curved surfaces.

Discussion—This model points to the notion that increasing curvature induces epithelial fluidization and cellular migration. This effect is not due to changes in the local mechanism of cell intercalation, which is independent of curvature, but rather to changes in the global structure of the cell junction network, which becomes less rigid with increased curvature. Cell rearrangements become energetically advantageous at higher curvatures, resulting in cellular configurations that are more malleable and more migratory.

Notably, part of our results is supported by two recent works using the spherical VM [67, 68]. Differently from these studies, however, our work is the first to 1) investigate the effect of curvature on both tissue's mechanical stability and cellular migratory behavior and 2) identify its underlying mechanism. In doing so, we offer testable hypotheses about how tissue mechanics respond to substrate curvature. For example, recent experiments on lung alveolospheres have shown that curvature enhances fluidity by modifying the distribution of cell packing [36]. Our study demonstrates that alterations in tissue contact topology affect the rate of cell rearrangements, providing a mechanistic framework for understanding these experimental results. Moreover, our results suggest that measuring junctional tensions (for example via localised laser ablation [69] or laser tweezers [70]) can serve as a direct indicator of tissue rigidity on curved surfaces. This new predictive metric could be employed to distinguish between different mechanical phases in organoid models. These findings provide the basis for future studies on more complex geometries with non-uniform curvatures, such as tubes, ellipsoids, and toroids.

The authors acknowledge the support of the Northeastern University Discovery Cluster. D.B. acknowledges support from the National Science Foundation (grant no. DMR-2046683), the Alfred P. Sloan Foundation, and The Human Frontier Science Program. JJF acknowledges support from the National Heart Lung and Blood Institute (grant no. NHLBI 1R01HL148152 and T32HL007118).

* Corresponding author: d.bi@northeastern.edu

[1] Peter Friedl and Darren Gilmour, "Collective cell migration in morphogenesis, regeneration and cancer," Nature reviews Molecular cell biology **10**, 445–457 (2009).

[2] Pernille Rorth, "Collective cell migration," Annual review of cell and developmental biology **25**, 407–429 (2009).

[3] Lior Atia, Dapeng Bi, Yasha Sharma, Jennifer A Mitchel, Bomi Gweon, Stephan A Koehler, Stephen J DeCamp, Bo Lan, Jae Hun Kim, Rebecca Hirsch, et al., "Geometric constraints during epithelial jamming," Nature physics **14**, 613–620 (2018).

[4] Jin-Ah Park, Lior Atia, Jennifer A Mitchel, Jeffrey J Fredberg, and James P Butler, "Collective migration and cell jamming in asthma, cancer and development," Journal of cell science **129**, 3375–3383 (2016).

[5] Jin-Ah Park, Jae Hun Kim, Dapeng Bi, Jennifer A Mitchel, Nader Taheri Qazvini, Kelan Tantisira, Chan Young Park, Maureen McGill, Sae-Hoon Kim, Bomi Gweon, et al., "Unjamming and cell shape in the asthmatic airway epithelium," Nature materials **14**, 1040–1048 (2015).

[6] Jennifer A Mitchel, Amit Das, Michael J O'Sullivan, Ian T Stancil, Stephen J DeCamp, Stephan Koehler, Oscar H Ocaña, James P Butler, Jeffrey J Fredberg, M Angela Nieto, et al., "In primary airway epithelial cells, the unjamming transition is distinct from the epithelial-to-mesenchymal transition," Nature communications **11**, 1–14 (2020).

[7] Lior Atia, Jeffrey J Fredberg, Nir S Gov, and Adrian F Pegoraro, "Are cell jamming and unjamming essential in tissue development?" Cells & development , 203727 (2021).

[8] Linda Oswald, Steffen Grosser, David M Smith, and Josef A Käs, "Jamming transitions in cancer," Journal of physics D: Applied physics **50**, 483001 (2017).

[9] Jin-Ah Park and Jeffrey J Fredberg, "Cell jamming in the airway epithelium," Annals of the American Thoracic Society **13**, S64–S67 (2016).

[10] Adrian F Pegoraro, Jeffrey J Fredberg, and Jin-Ah Park, "Problems in biology with many scales of length: Cell–cell adhesion and cell jamming in collective cellular migration," Experimental cell research **343**, 54–59 (2016).

[11] Monirosadat Sadati, Nader Taheri Qazvini, Ramaswamy Krishnan, Chan Young Park, and Jeffrey J Fredberg, "Collective migration and cell jamming," Differentiation **86**, 121–125 (2013).

[12] Margherita De Marzio, Ayşe Kılıç, Enrico Maiorino, Jennifer A Mitchel, Chimwemwe Mwase, Michael J O'Sullivan, Maureen McGill, Robert Chase, Jeffrey J Fredberg, Jin-Ah Park, et al., "Genomic signatures of the unjamming transition in compressed human bronchial epithelial cells," Science Advances **7**, eabf1088 (2021).

[13] Thomas E Angelini, Edouard Hannezo, Xavier Trepat, Manuel Marquez, Jeffrey J Fredberg, and David A Weitz, "Glass-like dynamics of collective cell migration," Proceedings of the National Academy of Sciences **108**, 4714–4719 (2011).

[14] Kenechukwu David Nnetu, Melanie Knorr, Steve Pawlizak, Thomas Fuhs, and Josef A Käs, "Slow and anomalous dynamics of an mcf-10a epithelial cell monolayer," Soft matter **9**, 9335–9341 (2013).

[15] Shao-Zhen Lin, Wu-Yang Zhang, Dapeng Bi, Bo Li, and Xi-Qiao Feng, "Energetics of mesoscale cell turbulence in two-dimensional monolayers," Communications Physics **4**, 1–9 (2021).

[16] Juan P Garrahan, "Dynamic heterogeneity comes to life," Pro-

ceedings of the national academy of sciences **108**, 4701–4702 (2011).

[17] Ricard Alert and Xavier Trepat, "Physical models of collective cell migration," arXiv preprint arXiv:1905.07675 (2019).

[18] Dapeng Bi, JH Lopez, Jennifer M Schwarz, and M Lisa Manning, "A density-independent rigidity transition in biological tissues," Nature Physics **11**, 1074–1079 (2015).

[19] Dapeng Bi, Jorge H Lopez, Jennifer M Schwarz, and M Lisa Manning, "Energy barriers and cell migration in densely packed tissues," Soft matter **10**, 1885–1890 (2014).

[20] Dapeng Bi, Xingbo Yang, M Cristina Marchetti, and M Lisa Manning, "Motility-driven glass and jamming transitions in biological tissues," Physical Review X **6**, 021011 (2016).

[21] Tamás Vicsek, András Czirók, Eshel Ben-Jacob, Inon Cohen, and Ofer Shochet, "Novel type of phase transition in a system of self-driven particles," Physical review letters **75**, 1226 (1995).

[22] Silke Henkes, Yaouen Fily, and M Cristina Marchetti, "Active jamming: Self-propelled soft particles at high density," Physical Review E **84**, 040301 (2011).

[23] M Chiang and D Marenduzzo, "Glass transitions in the cellular potts model," EPL (Europhysics Letters) **116**, 28009 (2016).

[24] Michael Czajkowski, Daniel M Sussman, M Cristina Marchetti, and M Lisa Manning, "Glassy dynamics in models of confluent tissue with mitosis and apoptosis," Soft matter **15**, 9133–9149 (2019).

[25] Xinzhi Li, Amit Das, and Dapeng Bi, "Mechanical heterogeneity in tissues promotes rigidity and controls cellular invasion," Physical review letters **123**, 058101 (2019).

[26] Hannah G Yevick, Guillaume Duclos, Isabelle Bonnet, and Pascal Silberzan, "Architecture and migration of an epithelium on a cylindrical wire," Proceedings of the National Academy of Sciences **112**, 5944–5949 (2015).

[27] Tianchi Chen, Andrew Callan-Jones, Eduard Fedorov, Andrea Ravasio, Agustí Brugués, Hui Ting Ong, Yusuke Toyama, Boon Chuan Low, Xavier Trepat, Tom Shemesh, et al., "Large-scale curvature sensing by directional actin flow drives cellular migration mode switching," Nature physics **15**, 393–402 (2019).

[28] Maxime Vassaux, Laurent Pieuchot, Karine Anselme, Maxence Bigerelle, and Jean-Louis Milan, "A biophysical model for curvature-guided cell migration," Biophysical journal **117**, 1136–1144 (2019).

[29] Alexandros Glentis, Carles Blanch-Mercader, Lakshmi Balasubramaniam, Thuan Beng Saw, Joseph d'Alessandro, Sebastien Janel, Audrey Douanier, Benedicte Delaval, Frank Lafont, Chwee Teck Lim, et al., "The emergence of spontaneous coordinated epithelial rotation on cylindrical curved surfaces," Science Advances **8**, eabn5406 (2022).

[30] Tom Brandstätter, David B Brückner, Yu Long Han, Ricard Alert, Ming Guo, and Chase P Broedersz, "Curvature induces active velocity waves in rotating multicellular spheroids," arXiv preprint arXiv:2110.14614 (2021).

[31] Maike Werner, Nicholas A Kurniawan, Gabriela Korus, Carlijn VC Bouten, and Ansgar Petersen, "Mesoscale substrate curvature overrules nanoscale contact guidance to direct bone marrow stromal cell migration," Journal of The Royal Society Interface **15**, 20180162 (2018).

[32] Pablo Rougerie, Laurent Pieuchot, Rafaela Silva Dos Santos, Julie Marteau, Maxence Bigerelle, Pierre-François Chauvy, Marcos Farina, and Karine Anselme, "Topographical curvature is sufficient to control epithelium elongation," Scientific reports **10**, 1–14 (2020).

[33] Wang Xi, Surabhi Sonam, Thuan Beng Saw, Benoit Ladoux, and Chwee Teck Lim, "Emergent patterns of collective cell migration under tubular confinement," Nature communications **8**, 1–15 (2017).

[34] Caterina Tomba, Valeriy Luchnikov, Luca Barberi, Carles Blanch-Mercader, and Aurélien Roux, "Epithelial cells adapt to curvature induction via transient active osmotic swelling," Developmental Cell (2022).

[35] Hannah Yevick, Guillaume Duclos, Isabelle Bonnet, and Pascal Silberzan, "The effects of out of plane curvature on collective cell migration," Biophysical Journal **106**, 357a (2014).

[36] Wenhui Tang, Amit Das, Adrian F Pegoraro, Yu Long Han, Jessie Huang, David A Roberts, Haiqian Yang, Jeffrey J Fredberg, Darrell N Kotton, Dapeng Bi, et al., "Collective curvature sensing and fluidity in three-dimensional multicellular systems," Nature Physics **18**, 1371–1378 (2022).

[37] Alexander G Fletcher, Miriam Osterfield, Ruth E Baker, and Stanislav Y Shvartsman, "Vertex models of epithelial morphogenesis," Biophysical journal **106**, 2291–2304 (2014).

[38] Silvanus Alt, Poulami Ganguly, and Guillaume Salbreux, "Vertex models: from cell mechanics to tissue morphogenesis," Philosophical Transactions of the Royal Society B: Biological Sciences **372**, 20150520 (2017).

[39] Bruno Monier, Melanie Gettings, Guillaume Gay, Thomas Mangeat, Sonia Schott, Ana Guarner, and Magali Suzanne, "Apico-basal forces exerted by apoptotic cells drive epithelium folding," Nature **518**, 245–248 (2015).

[40] Yasuhiro Inoue, Makoto Suzuki, Tadashi Watanabe, Naoko Yasue, Itsuki Tateo, Taiji Adachi, and Naoto Ueno, "Mechanical roles of apical constriction, cell elongation, and cell migration during neural tube formation in xenopus," Biomechanics and modeling in mechanobiology **15**, 1733–1746 (2016).

[41] Mototsugu Eiraku, Nozomu Takata, Hiroki Ishibashi, Masako Kawada, Eriko Sakakura, Satoru Okuda, Kiyotoshi Sekiguchi, Taiji Adachi, and Yoshiki Sasai, "Self-organizing optic-cup morphogenesis in three-dimensional culture," Nature **472**, 51–56 (2011).

[42] Daniel L. Barton, Silke Henkes, Cornelis J. Weijer, and Rastko Sknepnek, "Active vertex model for cell-resolution description of epithelial tissue mechanics," PLOS Computational Biology **13**, 1–34 (2017).

[43] Amit Das, Srikanth Sastry, and Dapeng Bi, "Controlled neighbor exchanges drive glassy behavior, intermittency, and cell streaming in epithelial tissues," Physical Review X **11**, 041037 (2021).

[44] Tatsuzo Nagai and Hisao Honda, "A dynamic cell model for the formation of epithelial tissues," Philosophical Magazine B **81**, 699–719 (2001).

[45] Reza Farhadifar, Jens-Christian Röper, Benoit Aigouy, Suzanne Eaton, and Frank Jülicher, "The influence of cell mechanics, cell-cell interactions, and proliferation on epithelial packing," Current Biology **17**, 2095–2104 (2007).

[46] Douglas B Staple, Reza Farhadifar, J-C Röper, Benoit Aigouy, Suzanne Eaton, and Frank Jülicher, "Mechanics and remodelling of cell packings in epithelia," The European Physical Journal E **33**, 117–127 (2010).

[47] Lars Hufnagel, Aurelio A Teleman, Hervé Rouault, Stephen M Cohen, and Boris I Shraiman, "On the mechanism of wing size determination in fly development," Proceedings of the National Academy of Sciences **104**, 3835–3840 (2007).

[48] Steven M Zehnder, Melanie Suaris, Madisonclaire M Bellaire, and Thomas E Angelini, "Cell volume fluctuations in mdck monolayers," Biophysical journal **108**, 247–250 (2015).

[49] M Lisa Manning, Ramsey A Foty, Malcolm S Steinberg, and Eva-Maria Schoetz, "Coaction of intercellular adhesion and cortical tension specifies tissue surface tension," Proceedings of

the National Academy of Sciences **107**, 12517–12522 (2010).
[50] Kenneth A Brakke, "The surface evolver," Experimental mathematics **1**, 141–165 (1992).
[51] Carl T Kelley, Iterative methods for optimization (SIAM, 1999).
[52] Le Yan and Dapeng Bi, "Multicellular rosettes drive fluid-solid transition in epithelial tissues," Phys. Rev. X **9**, 011029 (2019).
[53] Nicoletta I Petridou, Bernat Corominas-Murtra, Carl-Philipp Heisenberg, and Edouard Hannezo, "Rigidity percolation uncovers a structural basis for embryonic tissue phase transitions," Cell **184**, 1914–1928 (2021).
[54] Lara Carvalho, Pedro Patricio, Susana Ponte, Carl-Philipp Heisenberg, Luis Almeida, André S Nunes, Nuno AM Araújo, and Antonio Jacinto, "Occluding junctions as novel regulators of tissue mechanics during wound repair," Journal of Cell Biology **217**, 4267–4283 (2018).
[55] Elise Walck-Shannon and Jeff Hardin, "Cell intercalation from top to bottom," Nature reviews Molecular cell biology **15**, 34–48 (2014).
[56] Kenneth D Irvine and Eric Wieschaus, "Cell intercalation during drosophila germband extension and its regulation by pair-rule segmentation genes," Development **120**, 827–841 (1994).
[57] Robert J Tetley, Michael F Staddon, Davide Heller, Andreas Hoppe, Shiladitya Banerjee, and Yanlan Mao, "Tissue fluidity promotes epithelial wound healing," Nature physics **15**, 1195–1203 (2019).
[58] Masazumi Tada and Carl-Philipp Heisenberg, "Convergent extension: using collective cell migration and cell intercalation to shape embryos," Development **139**, 3897–3904 (2012).
[59] Matteo Rauzi, "Cell intercalation in a simple epithelium," Philosophical Transactions of the Royal Society B **375**, 20190552 (2020).
[60] Meryl A Spencer, Zahera Jabeen, and David K Lubensky, "Vertex stability and topological transitions in vertex models of foams and epithelia," The European Physical Journal E **40**, 1–17 (2017).
[61] Preeti Sahu, Janice Kang, Gonca Erdemci-Tandogan, and M Lisa Manning, "Linear and nonlinear mechanical responses can be quite different in models for biological tissues," Soft Matter **16**, 1850–1856 (2020).
[62] Denis L Weaire and Stefan Hutzler, The physics of foams (Oxford University Press, 1999).
[63] Preeti Sahu, Daniel M Sussman, Matthias Rübsam, Aaron F Mertz, Valerie Horsley, Eric R Dufresne, Carien M Niessen, M Cristina Marchetti, M Lisa Manning, and Jen M Schwarz, "Small-scale demixing in confluent biological tissues," Soft Matter **16**, 3325–3337 (2020).
[64] Rastko Sknepnek and Silke Henkes, "Active swarms on a sphere," Physical Review E **91**, 022306 (2015).
[65] András Szabó, R Ünnep, Eld Méhes, WO Twal, WS Argraves, Y Cao, and András Czirók, "Collective cell motion in endothelial monolayers," Physical biology **7**, 046007 (2010).
[66] Benoit Ladoux, René-Marc Mège, and Xavier Trepat, "Front–rear polarization by mechanical cues: From single cells to tissues," Trends in cell biology **26**, 420–433 (2016).
[67] Daniel M. Sussman, "Interplay of curvature and rigidity in shape-based models of confluent tissue," Phys. Rev. Research **2**, 023417 (2020).
[68] Evan Thomas and Sevan Hopyan, "Shape driven confluent rigidity transition in curved biological tissues," (2022).
[69] Rodrigo Fernandez-Gonzalez, Sérgio de Matos Simoes, Jens-Christian Röper, Suzanne Eaton, and Jennifer A Zallen, "Myosin ii dynamics are regulated by tension in intercalating cells," Developmental cell **17**, 736–743 (2009).
[70] Kapil Bambardekar, Raphaël Clément, Olivier Blanc, Claire Chardès, and Pierre-François Lenne, "Direct laser manipulation reveals the mechanics of cell contacts in vivo," Proceedings of the National Academy of Sciences **112**, 1416–1421 (2015).

Supplemental Materials for Epithelial layer fluidization by curvature-induced unjamming

SIMULATION DETAILS

To initialize the simulation, the vertex positions are generated via a Voronoi tesselation of a random set of points uniformly distributed on the sphere. A two-step minimization procedure is implemented to derive tissue equilibrium configurations. Using the open-source software Surface Evolver [50], we first minimize Eq.1 at $p_0^{in} = 3.695$ through a combination of the first-order conjugate-gradient and second-order Newton's method [51]. In this step, the contact topology is updated via T1s transitions [18, 19, 43, 60, 62]. T1 transitions are performed in sequence on edges with lengths $L < L_{min} = \{0.01, 0.02, 0.05, 0.1, 0.2, 0.3\}$ and this process is iterated four times. At each T1 transition, cells swap neighbors and the global edge network is relaxed via energy minimization. After this step, we increase the preferred shape index to $p_0 = 4$ and progressively decrease it by intervals $\Delta p_0 = 0.005$. At each intermediate p_0, the system's energy is minimized by allowing only vertex rearrangements. In this step, the contact topology remains fixed. Overall, this procedure generates a set of equilibrium configurations ranging $p_0 = 3.5 - 4$ and having the same contact topology. We analyze these ground states in spherical VMs with N ranging $36 - 300$. For each choice of the parameters (N, p_0), 200 initial states are randomly generated and equilibrated.

ANALYSIS OF PERCOLATION OF THE TENSION NETWORK

For each of the 200 equilibrium configurations with given (N, p_0), we extract the subset of edges with $\tau > 1e^{-20}$. These edges define the tissue's tension network. In the main text, snapshots of the tension network show that the network changes its size and connectivity by varying p_0 and N. To investigate the tension percolation state at different (p_0, N), we compute the largest connected component (LCC) of each network and check if the LCC has percolated. We define a percolating LCC as a cluster in which the maximum cartesian distance between each vertex pair is larger than $2R - \sqrt{\langle A \rangle}$, with R the sphere's radius and $\langle A \rangle$ the average cell area. In this way, a percolating LCC spans at least half of the sphere. For a given choice of (N, p_0), the tension percolation probability $P_{perc}(N, p_0)$ is defined as the fraction of tension networks that has percolated. We repeat this process for multiple p_0 and N, as shown in Fig.2b in the main text.

We further compute the percolation threshold $p_0^*(N)$ for each N. The percolation threshold $p_0^*(N)$ is defined such that $P_{perc}(N, p_0^*) = 0.5$, i.e. half of the 200 random seeds have percolated. After shifting $P_{perc}(N, p_0)$ by its relative $p_0^*(N)$, we calculate the scaling exponent ν as the value at which $P_{perc}(N, p_0 - p_0^*(N))$ collapses onto a single curve, as shown in the inset of Fig.2b.

CALCULATION OF ENERGY BARRIER ASSOCIATED WITH A T1 TRANSITION

Under confluent conditions, cells swap neighbors by reorienting their local connectivity network. This intercalation process is referred to as a T1 transition. During a T1 transition, an existing edge is collapsed into a fourfold vertex to create a new junction in the perpendicular orientation (Fig.3 a). For each of the 200 states with given (N, p_0), we perform a T1 transition on each edge of the spherical layer. To do so, we first collapse the edge and then equilibrate the system by keeping the fourfold vertex fixed. We calculate the correspondent ΔU as the difference in tissue's mechanical energy between the T1's initial state (right panel of Fig.3 a), where the edge has length $L(E) = L$, and the collapsed state (central panel of Fig.3 a), where $L(E) = 0$.

By construction, ΔU can be decomposed into two contributions (Supp. Fig.S1a): a topological contribution ΔU_{top}, which corresponds to the increase in the system's mechanical energy following the geometric collapse of the edge into a vertex (central panel of Supp. Fig.S1a); a relaxation contribution ΔU_{rel}, which corresponds to the decrease in the system's mechanical energy following the vertices rearrangements into a new equilibrium state (right panel of Supp. Fig.S1a). For each T1 transition, we calculate ΔU_{top} and ΔU_{rel} separately and analyze their statistics. We find that $\Delta U_{top} > \Delta U_{rel}$ in every T1 transition (Supp. Fig.S1b) and the two contributions are linearly correlated $\Delta U_{rel} = \eta \Delta U_{top}$, where $\eta = 0.68$ (inset of Supp. Fig.S1b).

MEAN FIELD MODEL OF T1 TRANSITIONS IN THE SPHERICAL VM

To understand the functional dependence of ΔU from (L, τ), we develop a mean-field model wherein all four cells involved in the T1 transition are regular hexagons (Supp. Fig.S1c). The pure topological collapse affects only the collapsed edge E and the four edges sharing vertices with E (edges a, b, c, d in Supp. Fig.S1c). Given an initial length $L(E) = L$, $L(a) = L(b) = L(c) = L(d) = L$. When E is collapsed into a fourfold vertex, the new length of the four edges becomes:

$$L(\alpha) = \sqrt{L(a)^2 + \frac{L^2}{4} - L(a)Lcos(k)}, \tag{6}$$

where k is the angle between a and E. Since $k = \frac{4}{6}\pi$ in regular hexagons and $L(a) = L$, Eq. 6 reduces to:

$$L(\alpha) = L(\beta) = L(\gamma) = L(\delta) = L\sqrt{\frac{5}{4} - cos\left(\frac{4}{6}\pi\right)}. \tag{7}$$

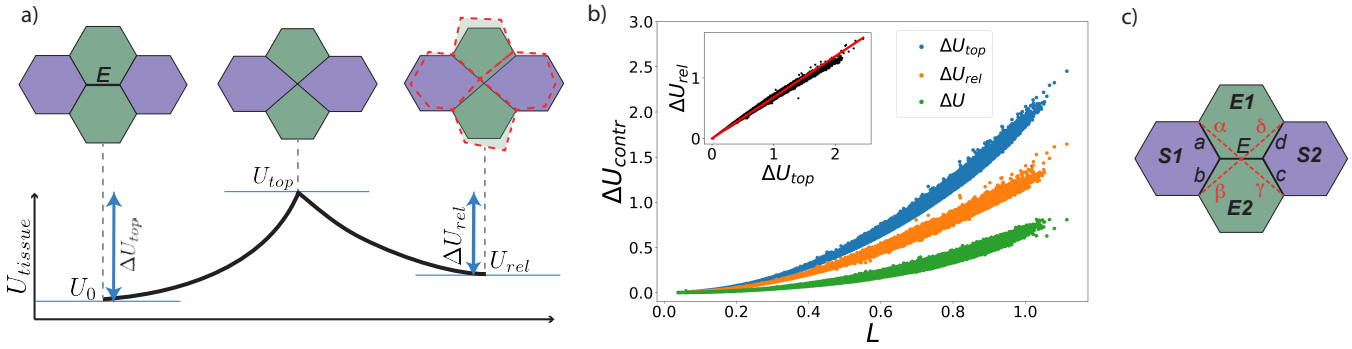

FIG. S1. a) Schematic of the tissue's energy profile associated with the topological and relaxation contributions. In the initial state, two adjacent cells (colored in green) share an edge E (left panel). When E is collapsed into a fourfold vertex while keeping the other vertices fixed, the tissue's energy increases to U_{top} (central panel). After the topological collapse, the layer rearranges the surrounding vertices and relaxes into a new state with lower energy U_{rel} (right panel). This rearrangement involves vertices belonging to other cells beyond the four cells involved in the T1 (not shown in the figure). b) T1's energy contributions versus L. At each T1, ΔU_{top} is always larger than ΔU_{rel}. ΔU_{rel} is well fitted by the linear function $\Delta U_{rel} = \eta \Delta U_{top}$ (red line in the inset). c) Schematic of the T1's topological collapse in a mean-field model with four regular hexagons. The geometric collapse of the edge E into a fourfold vertex affects only the four edges (a,b,c,d) sharing a vertex with E.

By definition, $\Delta U_{top} = \Delta U_{per} + \Delta U_{area}$, where:

$$\Delta U_{per} = \sum_{i\in\{S_1,S_2,E_1,E_2\}} (p_i^{fin} - p_0)^2 - (p_i^{in} - p_0)^2 \quad (8)$$

$$= \sum_{i\in\{S_1,S_2,E_1,E_2\}} \Delta p_i^2 + 2p_i^{in}\Delta p_i - 2\Delta p_i p_0. \quad (9)$$

$\Delta p_i = p_i^{fin} - p_i^{in}$, where p_i^{in} and p_i^{fin} are the perimeter of the i-th cell before and after the topological collapse, respectively. Δp_i depends geometrically on L as follows:

$$\Delta p_{\{S_1,S_2\}} = -2L + 2L\sqrt{\frac{5}{4} - cos(\frac{4}{6}\pi)} \quad (10)$$

$$\Delta p_{\{E_1,E_2\}} = -3L + 2L\sqrt{\frac{5}{4} - cos(\frac{4}{6}\pi)}. \quad (11)$$

Combining Eq. 9 with Eqs. 10 and 11 and defining the initial tension of the collapsed edge E as $\tau = p_{E1}^{in} + p_{E2}^{in} - 2p_0$, we arrive to the final equation:

$$\Delta U_{per} = AL^2 + BL + C\tau L. \quad (12)$$

The coefficients (A,B,C) are uniquely determined by the length L, angle k, and shape index p_0:

$$A = 16\left(\frac{5}{4} - cos\left(\frac{4}{6}\pi\right)\right) + 8\sqrt{\frac{5}{4} - cos\left(\frac{4}{6}\pi\right)} - 14 \quad (13)$$

$$B = 8p_0\left(1 - \sqrt{\frac{5}{4} - cos\left(\frac{4}{6}\pi\right)}\right) \quad (14)$$

$$C = 4\sqrt{\frac{5}{4} - cos\left(\frac{4}{6}\pi\right)} - 6. \quad (15)$$

Similarly, ΔU_{area} can be written as:

$$\Delta U_{area} = \sum_{i\in\{S_1,S_2,E_1,E_2\}} (a_i^{fin} - 1)^2 - (a_i^{in} - 1)^2 \quad (16)$$

$$= \sum_{i\in\{S_1,S_2,E_1,E_2\}} \Delta a_i^2 + 2a_i^{in}\Delta a_i - 2\Delta a_i, \quad (17)$$

where $\Delta a_i = a_i^{fin} - a_i^{in}$. The terms a_i^{in} and a_i^{fin} represent the area of the i-th cell before and after the topological collapse, respectively. For each of the four cells involved in the T1, the area difference Δa_i depends solely on the area of the triangle T_a formed by the three segments $\{a, \alpha, E/2\}$. Specifically:

$$\Delta a_{S_1,S_2} = 2T_a \quad (18)$$

$$\Delta a_{E_1,E_2} = -2T_a. \quad (19)$$

Combining Eq. 17 with Eqs. 18 and 19, ΔU_{area} reduces to:

$$\Delta U_{area} = 16T_a^2 = sin^2\left(\frac{4}{6}\pi\right)L^4. \quad (20)$$

Given that $\Delta U_{rel} = \eta \Delta U_{top}$ and $\Delta U = \Delta U_{top} - \Delta U_{rel}$, the final functional dependence of ΔU from (L,τ) can be written as:

$$\Delta U(L,\tau) = (1-\eta)\left(AL^2 + BL + C\tau L + sin^2\left(\frac{4}{6}\pi\right)L^4\right) \quad (21)$$

We have shown in the main text that the T1's energy barrier depends solely on the values of (L,τ) and is independent of the surface curvature. Supp. Fig.S2a displays the distribution of ΔU as a function of L at three different fixed values of $\tau = \{0.45, 0.5, 0.55\}$ and for four different radii of curvature $N = \{36, 48, 64, 72\}$ ($p_0 = 3.6$).

For each N and τ, $\Delta U(L)$ collapses on a single master curve independently of the radius of curvature. To account for deviations from the regular hexagonal structure, we fit the distribution $\Delta U(L,\tau)$ to Eq. 21 by setting the coefficients A, B, C

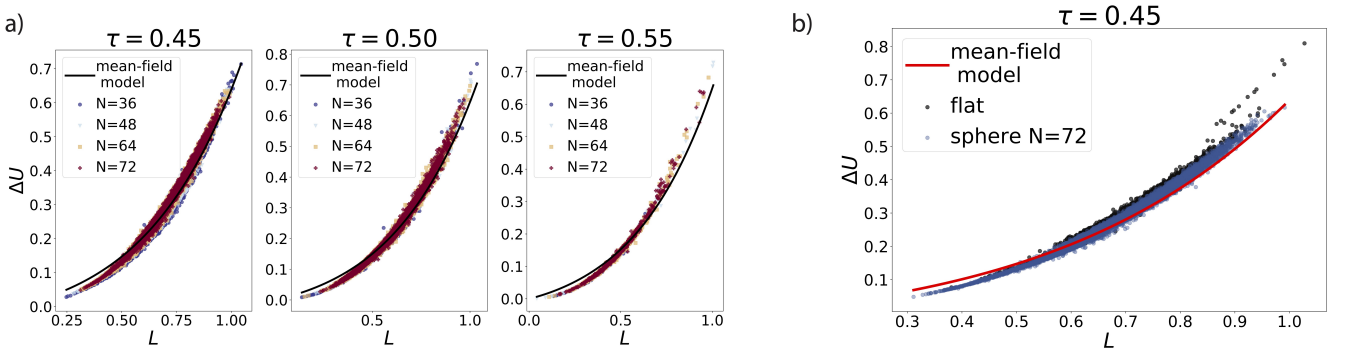

FIG. S2. a) T1's energy barriers ΔU versus L at fixed $\tau = \{0.45, 0.5, 0.55\}$. Different colors correspond to spheres with different numbers of cells $N = \{36, 48, 64, 72\}$. The target shape index is $p_0 = 3.6$. The black solid line represents the multivariate fit to Eq. 21. b) T1's energy barriers ΔU versus L at fixed $\tau = 0.45$ and $p_0 = 3.6$ in the flat VM ($N = 300$, black dots) and spherical VM ($N = 72$, blue dots). The red solid line represents the multivariate fit to Eq. 21 obtained on the spherical VM.

as fitting parameters. Notably, our mean-field model predicts correctly the functional dependence of the T1's energy barrier ΔU from the initial length and tension of the collapsed edge (L, τ) (black line in Supp. Fig.S2a).

To demonstrate that Eq.21 is independent of the layer's topology, we simulate a flat VM with $N = 300$ cells at $p_0 = 3.6$. We compute the T1's energy barriers ΔU using the same energy minimization scheme of the spherical VM. Supp. Fig.S2b shows the distribution $\Delta U(L)$ at fixed $\tau = 0.45$ for the flat VM (black dots) and spherical VM (blue dots). As predicted, both distributions collapse on the same master curve, confirming the universality of $\Delta U(L, \tau)$. Additionally, the fit to Eq. 21 obtained in the spherical VM predicts correctly the behavior of $\Delta U(L, \tau)$ on the flat layer (red solid line in Supp. Fig.S2b). As such, the functional dependence $\Delta U(L, \tau)$ predicted by our mean-field model represents a universal law that is independent of the surface topology.

DISTRIBUTION OF EDGE LENGTHS IN THE SPHERICAL AND FLAT VM

Fig.4b shows that edge lengths are stratified by a topological parameter Q that expresses the local connectivity around the edge. To demonstrate that edge lengths depend on the surrounding contact topology also in flat layers, we analyze their distribution in the flat VM at $p_0 = 3.6$. Analogous to the spherical layer, $P(L)$ appears as the sum of multiple Gaussian parametric in Q (Supp. Fig.S3a). Edges are shorter for larger Q, confirming that this behavior is independent of the layer's topology.

We analyze the distribution of edge lengths in spheres with different N. We find that curvature alters both the distribution of Q and L. For each Q, the average edge length μ_Q increases with increasing curvature (Supp. Fig.S3b). By increasing N, the proportion of edges with $Q > 0$ decreases while the one with $Q \leq 0$ increases (Supp. Fig.S3c). This hints at a key role of the hexagonal configuration (where $Z_{S1} = Z_{S2} = 6$ and

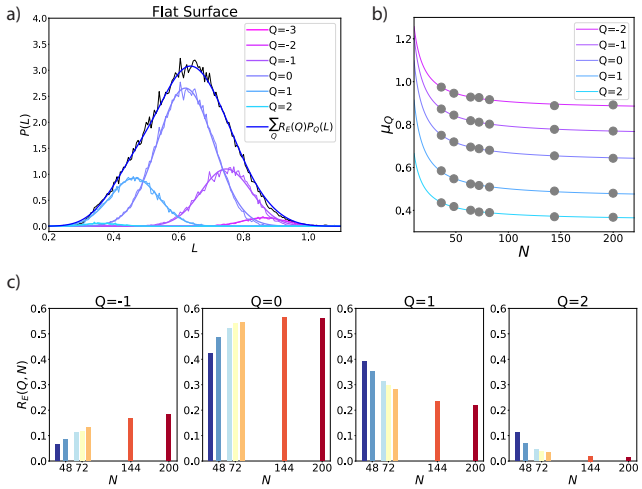

FIG. S3. a) Probability density of edge lengths L in the flat VM, stratified by Q. Each colored line represents the probability density $P_Q(L)$ of edge lengths with the same Q. For each $P_Q(L)$, the smooth line corresponds to its Gaussian fit $P_Q(L) = e^{(L-\mu_Q)/\sigma_Q}$. The black line corresponds to the total probability density $P(L)$. The underlying blue line is the weighted sum of the Gaussian fits for all Q. For each Q, the weight $R_E(Q,N)$ is given by the ratio between the number of edges with given Q and the total number of edges of the layer. b) Behavior of the average length μ_Q versus N on the spherical layer. c) Fraction of edges $R_E(Q,N)$ with given Q versus N on the spherical layer, for different values of Q.

$Q = 0$) not only in the layer's energetic stability [18, 46] but also in the contact topology of curved surfaces.

DEPENDENCE OF THE PERIMETER OF A SPHERICAL POLYGON ON CURVATURE

To understand the dependence of the edge lengths and tensions on the radius of curvature R (or equivalently on the number of cells N), we can propose a simple mean-field model. By

construction, the average solid angle Ω subtended by an individual cell depends on N as:

$$\Omega = 4\pi/N = R^{-2} \tag{22}$$

We first consider the simple case where the angle is subtended by a spherical cap of azimuthal angle θ. Although cells have polygonal boundaries rather than circular, we will show that this difference enters only as a different factor in our final predictions. The relationship between Ω and θ is given by:

$$\Omega = 4\pi \sin^2\left(\frac{\theta}{2}\right) \tag{23}$$

Additionally, the rim of the spherical cap has a perimeter given by:

$$P_{circle} = 2\pi R \sin\theta = 2\sqrt{\pi}\sqrt{1-\frac{1}{N}} \tag{24}$$

In the limit of large N, P_{circle} approaches the flat value of $\sqrt{4\pi} \approx 3.544$.

Eq.24 can be generalized to an arbitrary polygon. By substituting the factor $\sqrt{4\pi}$ with the term P_{flat} representing the polygon's perimeter on flat surfaces, we can extrapolate the curvature dependence of the perimeter $P(N)$ of a polygon on the sphere:

$$P(N) = P_{\text{flat}}\sqrt{1-\frac{1}{N}} = P_{\text{flat}}\sqrt{1-\frac{1}{4\pi R^2}}. \tag{25}$$

P_N decreases with decreasing N, and hence increasing curvature.

We have shown in the main text that the average edge tension $\langle\tau\rangle$ and length $\langle L\rangle$ have opposite behavior as a function of N. To demonstrate that the effect of curvature on the tension network governs the shift in the rigidity transition, we consider only the tension-dependent term τL of the energy barrier ΔU (see Eq.2). Based on Eq.3 and Eq.4:

$$\langle \Delta U\rangle \approx \langle L\rangle\langle\tau\rangle = 0 \Rightarrow p_0^*(N) = \langle P_{flat}\rangle\sqrt{1-1/N} \tag{26}$$

This dependence on N recapitulates the shift of the tension percolation threshold.

DYNAMIC VERTEX MODEL OF CELL MONOLAYERS ON A SPHERICAL SURFACE

In a recent work [36] by some of us, we have adapted our previously published dynamic vertex model [6] (DVM) on flat surfaces to study cellular dynamics in a confluent spherical monolayer. Here we utilize this spherical DVM to probe the effect of substrate curvature on the motility-driven unjamming transition. The model and the calculated dynamical quantities are described briefly below.

Energy Hamiltonian and single cell motility— The DVM Hamiltonian is described by the functional form of Eq.1. Cell motility is described by the overdamped equation of motion:

$$\Gamma\frac{d\vec{r}_i}{dt} = \vec{F}_i^{int} + v_0\hat{n}_i, \tag{27}$$

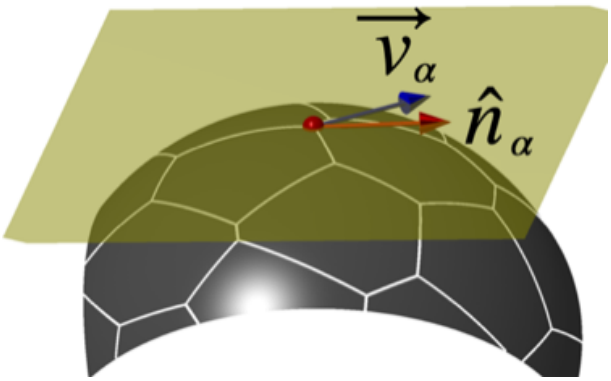

FIG. S4. The net velocity $\vec{v}_\alpha$ and the net direction vector $\hat{n}_\alpha$ of the vertex α are always projected on the tangent plane at the position $\vec{r}_\alpha$.

where $\vec{r}_i(t)$ is the position of the i-th vertex at time t, Γ is the frictional damping coefficient, $\vec{F}_i^{int}$ is the total cell-cell interaction force exerted on the i-th vertex, and $v_0\hat{n}_i$ represents the active motility force applied on the i-th vertex. The direction of $\hat{n}_i$ is determined by the sum of polarization vectors of the three cells sharing the vertex. The polarization vector of the m-th cell is given by $\hat{n}_m = (cos\theta_m, sin\theta_m)$, where the angle of polarization θ_m also exhibits an over-damped dynamics:

$$\frac{d\theta_m}{dt} = \eta, \qquad \langle\eta_i(t)\eta_j(t')\rangle = 2D_R\delta_{ij}\delta(t-t'). \tag{28}$$

η is a random variable obeying the statistics of Gaussian white noise with zero mean and variance $2D_R$. This description recapitulates the front-back polarity of migrating cells [20, 65, 66]. D_R is the rate at which the orientation of the cell polarization vector randomizes. At any point $\vec{x}$ on the sphere and at every time step, the displacements and the polarizations of the vertex positions are projected on the corresponding tangent plane. Given a vector $\vec{y}$ at a point $\vec{x}$ on the sphere, the projection operator $\vec{P}_T(\vec{x},\vec{y})$ is defined as [64]:

$$\vec{P}_T(\vec{x},\vec{y}) = \vec{y} - (\hat{x}\cdot\vec{y})\,\hat{x} \tag{29}$$

This exercise ensures that cells remain constrained on the spherical surface throughout the entire simulation (Supp. Fig.S4).

Simulation details—Simulations are initiated from the zero-motility ($v_0 = 0$) equilibrium configurations obtained through the minimization procedure described above. Given these configurations, finite motility ($v_0 > 0$) simulations are then performed. The vertex locations are updated through the Euler method according to Eq. 27. The time step of the simulations is $\Delta t = 0.02\tau$, where $\tau = \Gamma/K_P$ represents the unit of time in the DVM. We use Eq. 28 to determine the rotational noise on the cell polarizations.

In our simulations, T1 rearrangements are allowed with an embargo timer of 0.2τ when an edge is below a threshold length $l_c = 0.05\sqrt{A_0}$ [43]. We use Surface-Evolver [50] to

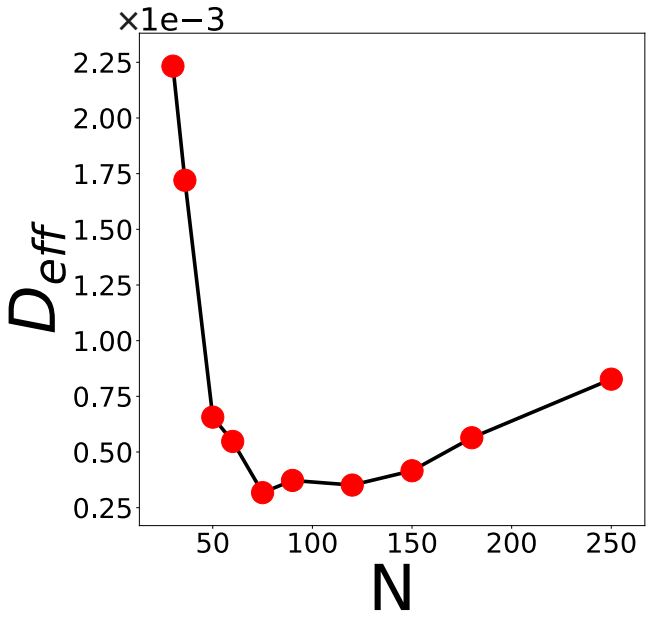

FIG. S5. Diffusion coefficient D_{eff} versus N extracted through linear fit of the MSD diffusive regime.

implement the DVM simulations. We perform DVM simulations of spheres with number of cells N ranging $30-250$. Analogous to the spherical VM, the radius of curvature of the spherical surface is chosen such that $R=\sqrt{N/4\pi}$. We examine the effect of curvature by varying the motility force v_0 in the range $0.02-0.14$ and keeping fixed the preferred shape index $p_0=3.65$ and the rotational noise strength $D_R=1$. In this way, the single cell dynamics remains Brownian. For each parameter set, we perform 10 independent simulations initiated from different random cell configurations.

From each simulation, we compute two different dynamical quantities. First, the average mean-square displacement (MSD) $\langle\Delta r^2(t)\rangle$ of cells as a function of time. In the MSD, distance is calculated based on the length of the geodesic curve connecting the initial and final position of the cell in the time interval t. We quantify the long-time diffusive behavior of the MSD by extracting the diffusion coefficient D_{eff}. Supp. Fig.S5 shows the behavior of D_{eff} at $v_0=0.09$ for different radii of curvature.

D_{eff} exhibits a strong dependence on N, decreasing dramatically with increasing N in the range $30-150$. A slight increase is observed for $N>150$ without exceeding the threshold of 10^{-3} that marks the fluid-to-solid transition [20, 63].

As shown in Fig.5b, we estimate D_{eff} for different values of v_0 and N.We also estimate the T1 transition's rate k_{T1}, defined as the number of neighbor exchanges per junction per unit of time.